gels

MDPI

Article

Microscopic Insight into Knudsen and Electromagnetic Effects on Thermal Conductivity of Closed Mesoporous Metal Gels

Haiyan Yu [1,*], Ning Guo [1], Anqi Chen [1], Mingdong Li [1], Haochun Zhang [2] and Mu Du [3,*]

[1] Institute of Thermal Science and Technology, Shandong University, Jinan 250061, China; 202334300@mail.sdu.edu.cn (N.G.); 202234272@mail.sdu.edu.cn (A.C.); 202414341.sdu@vip.163.com (M.L.)
[2] School of Energy Science and Engineering, Harbin Institute of Technology, Harbin 150001, China; hczhang@hit.edu.cn
[3] Institute for Advanced Technology, Shandong University, Jinan 250061, China
* Correspondence: yuhaiyan@sdu.edu.cn (H.Y.); dumu@sdu.edu.cn (M.D.)

Abstract

Accurate thermal characterization of closed mesoporous metal gels is vital for high-temperature uses, yet microscale effects often ignored in macroscopic models significantly impact heat transfer. This study introduces a new predictive method based on an equivalent Voronoi model, accounting for the Knudsen effect and microscale electromagnetic interactions. Predicted thermal conductivity closely matched experimental results, with an average error of 5.35%. The results demonstrate that thermal conductivity decreases with porosity, increases with temperature, and varies with pore size, with a minimum of 17.47 W/(m·K) observed at ~1 μm. Variations in refractive index, extinction coefficient, and specific surface area exert negligible influence. Conductive heat transfer is suppressed under Knudsen-dominated conditions at small pore sizes. Electromagnetic analysis around the pore size corresponding to minimum conductivity reveals localized surface plasmon resonances and magnetic coupling at the gas–solid interface, which enhance radiative dissipation and further reduce thermal conductivity. Radiation dissipation efficiency increases with decreasing porosity and pore size. This model thus serves as a predictive tool for designing high-performance thermal insulation systems for elevated-temperature applications.

Keywords: thermal conductivity; microscale heat transfer; mesoporous metal gels; microscale thermal radiation

Academic Editors: Juan Manuel Lázaro-Martínez and Michael Arkas

Received: 2 August 2025
Revised: 22 August 2025
Accepted: 11 September 2025
Published: 15 September 2025

Citation: Yu, H.; Guo, N.; Chen, A.; Li, M.; Zhang, H.; Du, M. Microscopic Insight into Knudsen and Electromagnetic Effects on Thermal Conductivity of Closed Mesoporous Metal Gels. *Gels* **2025**, *11*, 739. https://doi.org/10.3390/gels11090739

1. Introduction

Thermal insulators with precisely engineered microstructures are pivotal to meeting current demands for energy efficiency and temperature regulation [1]. Among these, closed mesoporous metallic gels (CMM-gels) exhibit low effective thermal conductivity and robust thermomechanical stability [2,3], making them promising for applications such as aerospace thermal barriers, thermal management of power-dense electronics, renewable-energy conversion hardware, and high-temperature protective coatings [4,5]. To quantify heat transport in CMM-gels, researchers compute the effective thermal conductivity and decompose it into equivalent conductive and radiative components [6,7]. For closed pores smaller than approximately 4 mm, convective heat transfer is generally considered negligible [8].

Understanding thermal transport in the CMM-gels requires separate consideration of conductive (κ_{cond}) and radiative (κ_{rad}) pathways due to their distinct underlying physics. For κ_{cond}, predictive approaches have evolved from empirically derived correlations [9],

which are highly sensitive to specific material morphologies, toward physics-based methodologies. The latter include analytical thermal resistance network modeling via equivalent circuit methods [10], later refined to capture nanoscale solid-phase phonon scattering [10–12] and gaseous Knudsen effects [13,14] in mesoporous systems [11,15], as well as sophisticated numerical simulations employing Finite Element Analysis [16,17], Molecular Dynamics [18], or the lattice Boltzmann method [19,20] on reconstructed/idealized geometries. In contrast, κ_{rad} dominates at elevated temperatures and microscale/submicron characteristic dimensions [21,22], where surface roughness, intra-cavity scattering, and sub-wavelength near-field coupling [23,24] dramatically enhance non-contact heat transfer. This micro-radiative complexity fundamentally challenges conventional modeling paradigms: Full Radiative Transfer Equation (RTE) solvers [25–27] become computationally prohibitive beyond simplified geometries; approximations neglecting absorption/scattering [25] sacrifice physical fidelity; and the widely adopted Rosseland diffusion approximation [26,28] fails catastrophically as radiative fluxes exceed blackbody predictions at small scales. Attempts have been made to modify the Rosseland approximation by incorporating correction factors or accounting for near-field effects, but a unified approach remains elusive [14,25,29–31]. Consequently, developing a precise model for the radiative thermal conductivity of CMM-gels is essential.

This research provides a theoretically grounded and computationally efficient tool for predicting thermal transport in CMM-gels. The equivalent Voronoi model was used as a physical model, the conductive equivalent thermal conductivity was generated based on the molecular dynamics method, and the radiative thermal conductivity was derived from the microscale radiation method. Using this integrated prediction approach, seven critical factors influencing thermal conductivity—including porosity, cell size, temperature, the refractive index, the extinction coefficient, pore shape, and surface area to volume ratio—were systematically investigated. The study revealed fundamental relationships between these parameters and thermal transport characteristics, identifying optimal conditions for thermal conductivity minimization. The transmission mechanism of microscale thermal radiation was analyzed by examining electromagnetic distributions at critical configurations. Electromagnetic analysis demonstrates enhanced radiative dissipation efficiency through interfacial resonance phenomena at gas–solid boundaries, which actively suppress thermal conductivity. Then, the transmission mechanism of microscale thermal radiation inside the pores was analyzed by finding the electromagnetic distribution of the thermal conductivity minimum point in porosity and pore size.

2. Models

2.1. Geometric Model

For most mesoporous materials, the matrix comprises an assembly of numerous small unit elements [31]. Owing to their inherent structural irregularity and heterogeneity, developing an accurate theoretical model to predict the thermal conductivity of such materials remains highly challenging. To better replicate the internal architecture of CMM-gels, this study employs a complex three-dimensional Voronoi model to represent the closed-cell structure. Voronoi-based architectures have garnered significant attention for their capacity to capture the randomness and complex mesoscale morphology of real porous materials [32].

The foam geometry is defined by a Voronoi tessellation of randomly placed seed points, yielding polyhedral cells bounded by surfaces equidistant from neighboring seeds. Formally, the Voronoi region $V(pi)$ associated with seed p_{i} is defined as [32]:

$$V(pi) = \{p \,|d(p, p_i) \leq d(p, p_j), j \neq i, j = 1, \ldots, n\} \quad (1)$$

where $V(pi)$ denotes the Voronoi cell associated with seed point pi (with i being the index of this "center seed point"), p represents any spatial position vector, $d(\cdot,\cdot)$ stands for the Euclidean distance metric, n corresponds to the total number of seed points in the domain, and j is the running index of all other seed points used for comparison in the Voronoi construction.

Evaluating the pairwise distances among seeds thus produces an irregular polyhedral lattice that more accurately captures the geometric complexity of porous substrates. Subsequently, a cell wall thickness d_w is assigned to each Voronoi cell. During the construction process, the intersecting boundaries between adjacent cells are defined as solid walls, which serve as critical structural supports within the overall architecture, ultimately forming CMM-gels, as shown in Figure 1. In this Voronoi model, the porosity φ is defined as the ratio of the total air volume to the total volume of the geometric computational domain. The equivalent pore diameter d_p is determined based on the average pore size, calculated using the domain volume V and the total number of seed points n, following the relation $d_p = V/n$. The equivalent cell size, D_h, is further defined as $D_h = d_p/\varphi$.

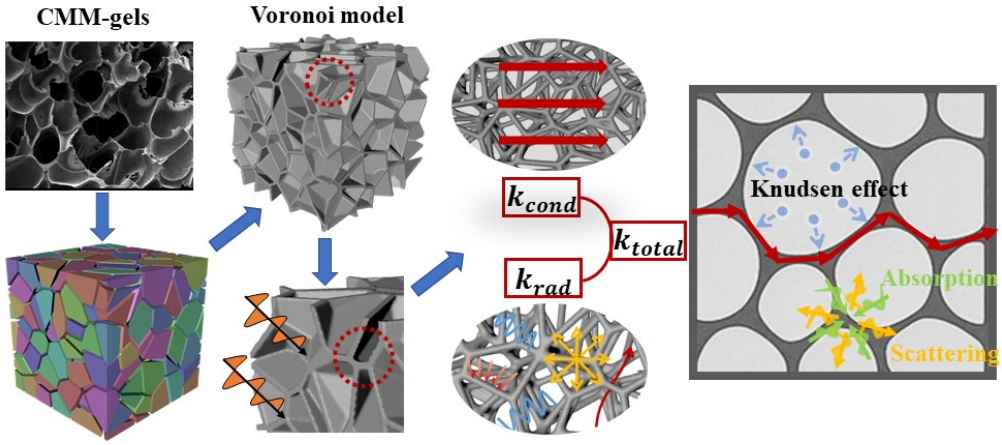

Figure 1. Schematic representation of the heat transfer model for CMM-gels.

2.2. Calculation Methods

In this work, the CMM-gels were represented by a Voronoi model, and the effective thermal conductivity was determined by solving the governing heat conduction equations together with Fourier's law. At micropore dimensions, conduction, radiation, and convection exhibit distinct behaviors, leading to significant variation in the overall thermal conductivity of porous materials [33,34]. When the characteristic pore diameter falls below 4 mm, density gradients in the confined air become negligible and the gas phase remains essentially stationary, so convective heat transfer can be neglected [35]. Consequently, only thermal conduction and thermal radiation are considered in the analysis. Therefore, the total effective thermal conductivity κ_{total} was expressed as follows [36]:

$$\kappa_{total} = \kappa_{cond} + \kappa_{rad} \quad (2)$$

where κ_{cond} denotes the conductive contribution and κ_{rad} is the radiative contribution to effective thermal conductivity. The computational framework for predicting the effective thermal conductivity of the CMM-gels is illustrated in Figure 2.

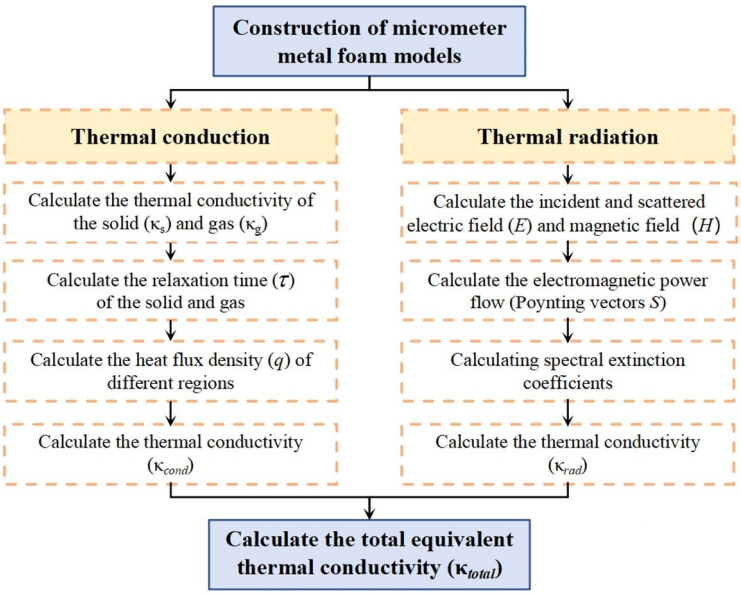

Figure 2. Flow diagram of the equivalent thermal conductivity calculation progress.

In the present work, the conductive thermal conductivity κ_{cond} is governed by Fourier's law and the energy conservation equation, yielding a transient partial differential equation in space and time. The domain comprises a metal-skeleton region and a gas region, each with its own density, specific heat capacity, and thermal conductivity. Heat transport in both regions is described by the following conjugate heat transfer equations [37]:

$$(\rho C_P)_s\left(\frac{\partial T}{\partial t}\right) = k_s\nabla^2 T \quad , \quad (\rho C_P)_f\left(\frac{\partial T}{\partial t}\right) = k_f\nabla^2 T \tag{3}$$

where ρ denotes the density, C_P represents the specific heat capacity, T is the local temperature, t stands for the time variable, ∇^2 denotes the Laplace operator, while k_s and k_f correspond to the thermal conductivities of the solid skeleton and the gas phase, respectively. At the microscale, when the characteristic size of the cellular structure approaches the mean free path of gas molecules, the Knudsen effect becomes significant, leading to the suppression of gas-phase thermal conduction [22]. The Knudsen effect refers to the phenomenon in which, as the pore size decreases, the frequency of intermolecular collisions is reduced during heat transport within confined gas domains, resulting in a decline in thermal conductivity [38]. Therefore, in calculating the gas-phase thermal conductivity in the CMM-gels, the influence of both pore size and the mean free path of gas molecules must be considered. The corrected expression for gas-phase thermal conductivity that incorporates these microscale effects is given as follows [39]:

$$k_f = \frac{k_{g0}}{1 + 2\beta K_n} \tag{4}$$

where $\kappa_{g,0}$ is the bulk gas thermal conductivity (0.026 $\mathrm{W{\cdot}m^{-1}{\cdot}K^{-1}}$ for air at 300 K and 1 bar) [40–42], and β is an energy accommodation coefficient (1.94 for air at 300 K and 1 bar) [39]. $Kn = \Lambda_g/d$ is the Knudsen number, which refers to the ratio of the mean free path of the air Λ_g(68 nm for air at 300 K and 1 bar) [39] to the cell size d.

In this study, the lattice Boltzmann method (LBM) is employed as the numerical solver to simulate the thermal conduction process in CMM-gels, with the D3Q19 model being used for its high numerical stability and accuracy. In this approach the temperature field is

represented by a set of distribution functions $f_i(x, t)$, each associated with one of nineteen discrete velocity vectors e_i. Their evolution obeys the collision–streaming equation [39]:

$$f_i(x + e_i\delta t, t + \delta t) - f_i(x, t) = -\frac{1}{\tau}[f_i(x, t) - f_i^{eq}(x, t)] \quad (5)$$

where f_i is the temperature distribution function in the i-th discrete direction at position x, δt is the time step, f_i^{eq} represents the local equilibrium distribution function, $T(x,t)$ is the local temperature, which is recovered as the zeroth moment, $T(x,t) = \sum_i f_i$, and τ is the dimensionless relaxation time that differs for the gas and solid phases and can be expressed as follows [40]:

$$\tau = \frac{3}{2}\frac{k_{s/f}}{\rho C_P c^2 \delta t} + 0.5 \quad (6)$$

where c represents the phonon group velocity. Isothermal walls were imposed via the non-equilibrium bounce-back scheme [40], while adiabatic boundaries were handled by a reflective Neumann condition [41]. After the lattice Boltzmann solver reached steady state, the heat-flux density q was extracted [42] using the following:

$$q = \frac{\tau - 0.5}{\tau}\left(\sum e_i f_i\right) \quad (7)$$

The effective conductive thermal conductivity κ_{cond} was then calculated as follows:

$$\kappa_{cond} = \frac{L \times \int q dA'}{\Delta T \int dA'} \quad (8)$$

where L represents the length of the computational domain, and A' is the cross-sectional area. In the following work, the κ_{cond} of the CMM-gels was determined using Equation (9). The radiative thermal conductivity κ_{rad} of CMM-gels is obtained by treating thermal radiation as an electromagnetic phenomenon via Maxwell's equations, which describe wave propagation and interaction with matter, as follows [42]:

$$\nabla \times E = -\frac{\partial B}{\partial t},\ \nabla \times H = J + \frac{\partial D}{\partial t} \quad (9)$$

where E is the electric field, H the magnetic field, B is the magnetic flux density, $B = \mu H$, μ presents the permeability, D is the electric displacement vector, $D = \varepsilon E$, ε is the permittivity, J is the current density, and $J = \sigma E$, and σ is the electrical conductivity. Perfectly matched layers were applied at the domain boundaries to absorb outgoing waves and eliminate non-physical reflections. From the complex field solution using the finite element method (FEM), the time-averaged Poynting vector S can be obtained as follows [43]:

$$S = \frac{1}{2}\cdot \mathrm{Re}\{E \times H^*\} \quad (10)$$

The Poynting vector can be used to calculate the incident and scattered electromagnetic fields, from which the corresponding incident power can be obtained. The relationship of absorption coefficient $\sigma_{a,\lambda}$ and the scattering coefficient $\sigma_{s,\lambda}$ serves as the basis for further evaluating the thermal radiative properties of the material, as follows [44]:

$$\sigma_{a,\lambda} = \frac{-Re\iint_\Sigma \left\{E^{(inc)} \times H^{(sca)*} + E^{(sca)} \times \left(H^{(inc)*} - H^{(sca)*}\right)\right\}\cdot n dA'}{N \cdot Re\left\{E^{(inc)} \times H^{(inc)*}\right\}} \quad (11)$$

$$\sigma_{s,\lambda} = \frac{Re \iint_{\Sigma} \left\{ E^{(inc)} \times H^{(sca)*} \right\} \cdot n dA'}{N \cdot Re \left\{ E^{(inc)} \times H^{(inc)*} \right\}} \tag{12}$$

where $E^{(sca)}$ and $H^{(sca)}$ represent the scattered electric and magnetic fields, respectively, and $E^{(inc)}$ and $H^{(inc)}$ denote the incident electric and magnetic fields, respectively. N is the unit normal vector to the surface area, Re indicates the real part of a complex number, and * denotes the complex conjugate. {TC "2.3.2 Thermal radiation thermal conductivity calculation"\1 3} The extinction coefficient $\sigma_{e,\lambda}$ is commonly used to characterize the overall energy loss during wave propagation and can be calculated as $\sigma_{e,\lambda} = \sigma_{s,\lambda} + \sigma_{a,\lambda}$. To further analyze the radiation mechanism of microscale thermal radiation, combined with the Beer–Lambert Law [45], the spectral absorptivity A can be obtained as $A = 1 - e^{-\sigma_{a,\lambda} \cdot L}$, and the spectral reflectivity R, calculated by $R = 1 - e^{-\sigma_{s,\lambda} \cdot L}$. In the Rosseland optical approximation, the Rosseland mean extinction coefficient $\sigma_{e,R}$ is employed to describe the overall absorption and scattering characteristics of a material with respect to electromagnetic waves, particularly thermal radiation. It is obtained by performing a weighted average of the spectral extinction coefficients and the radiative intensity over all frequencies [46]:

$$\frac{1}{\sigma_{e,R}} = \frac{\int_0^{\infty} \frac{1}{\sigma_{e,\lambda}} f(\lambda, T) d\lambda}{\int_0^{\infty} f(\lambda, T) d\lambda} \tag{13}$$

$f(\lambda, T)$ represents the spectral distribution of Planck blackbody radiation and indicates the fraction of radiative energy at a given wavelength relative to the total emitted energy [46]. By incorporating the $\sigma_{e,R}$ into the energy equation, the effective radiative thermal conductivity κ_{rad} can be calculated [47].

$$\kappa_{rad} = \frac{16 \sigma_{SB} {T_m}^3}{3 \sigma_{e,R}} \tag{14}$$

where σ_{SB} denotes the Stefan–Boltzmann constant. The κ_{rad} in this paper is obtained by Equation (14); combined with Equation (8), the total thermal conductivity κ_{total} can be finally obtained. In order to analyze the proportion of thermal radiation and thermal conduction in more detail, the radiation contribution ratio is defined as $\omega = \kappa_{rad} / \kappa_{total}$.

3. Results and Discussion

3.1. Model Verification

To evaluate the reliability of the prediction model, the experimental data from the two most common processing methods currently used, powder metallurgy [48] and foaming [49–51], were compared and verified, encompassing porosity values between 50% and 98%. As illustrated in Figure 3, the simulation results exhibit a high degree of consistency with the experimental data [48–51], with an average error of 5.35% and maximum deviation below 8.6%. This deviation can be partially attributed to slight variations in porosity (±2%) and pore size distribution (±5%) inherent to the fabrication processes of porous metals, as reported in the original experimental studies [48–51], as well as minor simplifications in the Voronoi model's geometric representation of complex real-world pore architectures. Moreover, the model accurately reproduces the observed dependence of thermal conductivity on porosity. These outcomes provide strong evidence for the credibility of the simulation method, which is subsequently adopted for detailed analysis of thermal transport in CMM-gels. Next, the impact factors' effect on this predicted thermal conductivity is discussed in detail in the following section.

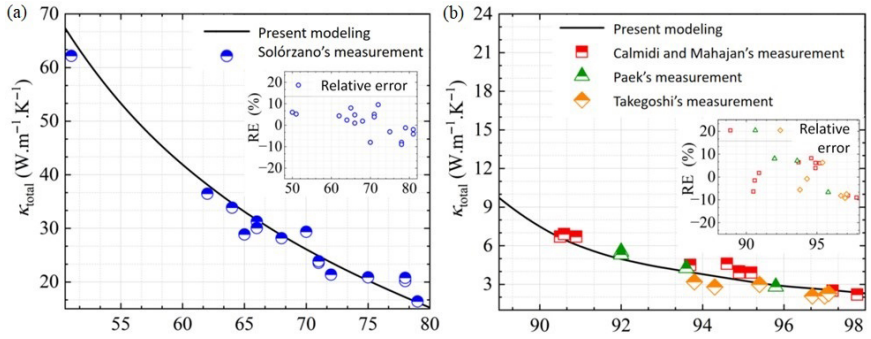

Figure 3. The comparison of the simulation results with the experimental data [48–51] under different processing: (**a**) powder metallurgy; (**b**) foaming.

3.2. Factors Influencing the Equivalent Thermal Conductivity

This section systematically analyzes the influence of various factors on the heat transfer properties of CMM-gels. Specifically, the effects of cell size (D_h = 0.1–100 μm), porosity (φ = 55–90%), temperature (T = 300–600 K), volumetric specific surface area ($VSSA$), refractive index n, and extinction coefficient k are investigated. Their impacts on the total thermal conductivity κ_{total}, the radiative thermal conductivity κ_{rad}, the conductive κ_{cond}, and the radiative contribution ratio ω in CMM-gels are discussed in detail, specifically using aluminum properties as a base case, adopting the optical properties from Rakić's experimental data [52].

3.2.1. Effect of the Cellular Structure

To investigate the effects of porosity and cell size on the thermal conductivity of CMM-gels, a total of 300 distinct models were generated with T = 300 K, 10 nm $\leq D_h \leq$ 100 μm, and 0.53 $\leq \varphi \leq$ 0.94. The corresponding κ_{total}, κ_{rad}, κ_{cond}, and ω are presented in Figure 4.

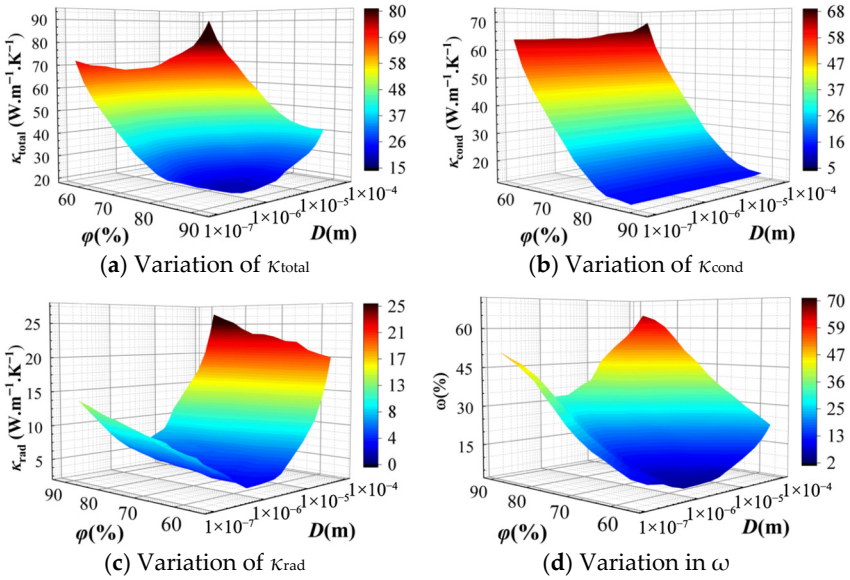

Figure 4. The thermal conductivity of CMM-gels versus cell size and porosity: (**a**) the total thermal conductivity; (**b**) the conductive thermal conductivity; (**c**) the radiative thermal conductivity; and (**d**) the radiative thermal conductivity proportion.

Figure 4a illustrates the variation in the κ_{cond} with respect to D_h and φ. The overall trend indicates that κ_{total} decreases significantly as φ increases. This is attributed to the reduction in the solid framework, which enhances the relative influence of the gas phase. In addition, as the D_h decreases, κ_{total} initially reaches a minimum, attaining its lowest value at

D_h = 1 μm, and then increases rapidly with further reduction in cell size. When the Knudsen effect is considered, Figure 4b presents that κ_{cond} decreases with increasing φ and decreasing D_h. The Knudsen effect indicates that, at the microscale, the thermal conductivity of the gas phase is significantly suppressed due to the reduced frequency of intermolecular collisions, which limits the gas's ability to transport heat. Consequently, smaller D_h leads to greater dependence on the solid framework for heat conduction, resulting in a further reduction in κ_{cond}. Moreover, in the closed cell, more intense collisions between gas molecules and the solid framework occur, leading to more pronounced variations in κ_{cond} compared to open-cell foams.

Figure 4c shows the variation in the κ_{rad} with the D_h under high porosity conditions. It can be observed that κ_{rad} initially decreases with decreasing D_h, reaches a minimum, and then increases as D_h continues to grow. This non-monotonic trend is attributed to the influence of microscale effects on radiative transfer. As the D_h decreases, particularly at the microscale, the radiative contribution becomes significantly enhanced. This enhancement arises because smaller D_h shorten the radiative path length and intensify electromagnetic resonance within the material. This effect is especially pronounced when the structural dimensions approach the characteristic wavelength of Planck's Law, where interference effects begin to dominate, leading to a marked variation in κ_{rad}. The contribution of κ_{cond} to the κ_{total} exceeds that of the κ_{rad}, as shown in Figure 4d. However, in high-porosity CMM-gels, as the cell walls become thinner and φ increases, κ_{rad} gradually becomes the dominant contributor to the overall thermal conductivity.

3.2.2. Effect of Temperature

Since the CMM-gels are mostly applied with significant temperature changes, in this section, seven randomly generated models with φ = 90% were selected to investigate the influence of temperature on the κ_{total}. The temperature range spans from 300 K to 600 K with an increment of 50 K. This analysis examines the variation of κ_{total} from room temperature to elevated temperatures. Based on experimental data [52], a temperature-dependent relationship for the thermal conductivity of solid aluminum was established, as illustrated in Figure 5.

As seen in Figure 5, when the T increases from 300 K to 600 K, both the κ_{total} and the κ_{rad} exhibit an increasing trend, which is consistent with the experimental results. κ_{cond} decreases with decreasing D_h, after which the decreasing trend becomes less pronounced. This behavior is attributed to the Knudsen effect, where the reduced frequency of intermolecular collisions significantly suppresses the thermal conductivity of the gas phase. As the D_h further decreases to the microscale or even nanoscale, the solid framework gradually dominates heat conduction, and the gas-phase contribution becomes negligible. Under these conditions, heat transfer is primarily governed by the solid matrix, leading to a slower variation in κ_{cond}. With increasing T, the rise in κ_{rad} becomes more significant. This is due to the shift in the blackbody radiation peak toward shorter wavelengths (higher energy) at elevated temperatures, resulting in increased radiative energy and, consequently, a higher κ_{total}. At a high T, κ_{rad} becomes the dominant contributor to the overall thermal conductivity. However, it is worth noting that when 0.6 μm < D_h < 2 μm, the κ_{total} reaches a minimum and remains nearly constant over an extended interval. This observation suggests the existence of an optimal D_h range, within which the κ_{total} is governed by a balanced interplay between D_h and φ, resulting in a stable minimum value. In the production and application of the CMM-gels, precise control over D_h is critical, which can help optimize κ_{total}, enabling the development of materials with superior thermal insulation performance.

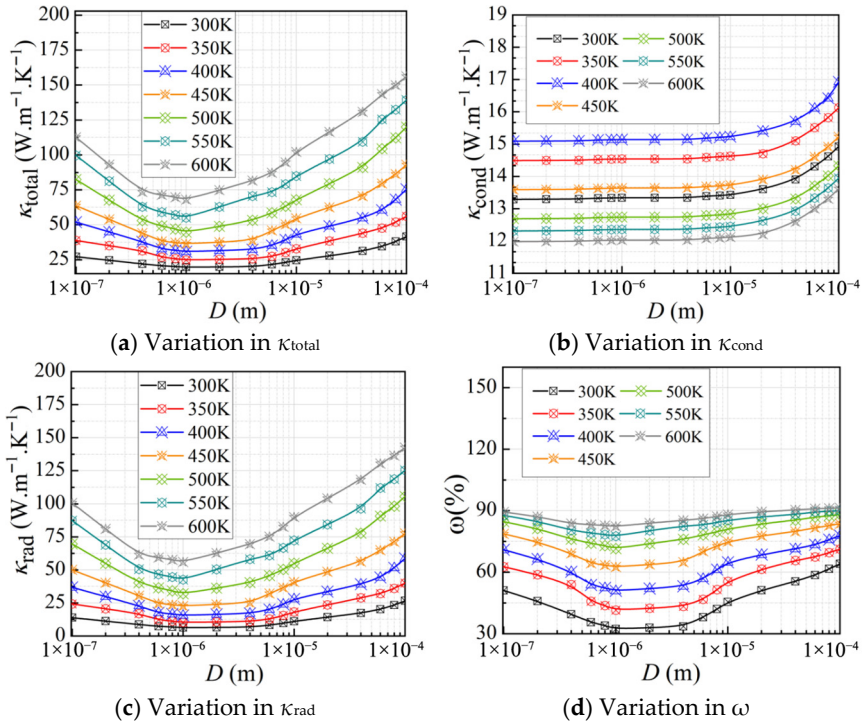

Figure 5. The equivalent thermal conductivity of CMM-gels versus cell size at different temperatures.

3.2.3. Effect of Volumetric Specific Surface Area

In these closed-pore models, the pore volume is maintained constant, and pores of different shapes are constructed within the CMM-gels to increase the overall surface area. As shown in Figure 6, when the D_h = 100 μm, the models with different closed-pore shapes are a tetrahedron (surface area of 47,313 μm^2), an octahedron (surface area of 45,538 μm^2), a dodecahedron (surface area of 44,604 μm^2), a tetradecahedron (surface area of 43,876 μm^2), and a cylinder (surface area of 43,472 μm^2). The volume-to-surface-area ratio (*VSSA*) of the models is obtained by comparing them with their volume. The order of volume-specific surface area from large to small is tetrahedron ($VSSA_1$), octagonal prism ($VSSA_2$), dodecaprism ($VSSA_3$), tetradecephalone ($VSSA_4$), and cylinder ($VSSA_5$), to explore the effect of different volume specific surface areas on the equivalent thermal conductivity of CMM-gels. These models were calculated at T = 300 K and φ = 90%.

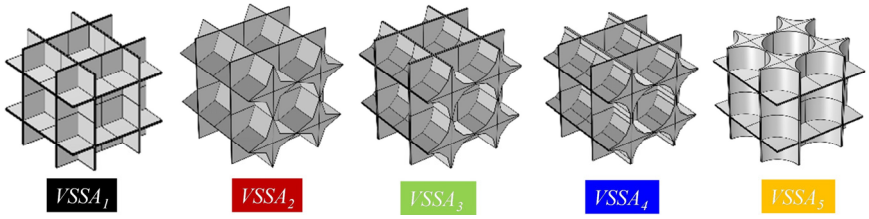

Figure 6. Illustration of volume-to-surface area ratios.

By introducing serrated structures on the outer surfaces of pores in CMM-gels, as shown in Figure 7, the *VSSA* can be significantly increased, which in turn influences the κ_{total}. At smaller D_h, the increase in *VSSA* enhances the thermal conduction capability of the solid framework. This is because the serrated structures not only provide a larger solid surface area but also intensify scattering effects at the gas–solid interface. As a result, the efficiency of conductive heat transfer is increased, leading to an improvement in the κ_{cond}, a phenomenon that becomes more pronounced as the characteristic size decreases. With increasing *VSSA*, the κ_{rad} exhibits a clear upward trend. The serrated structures enlarge

the surface area of the solid matrix and introduce additional regions for absorption and scattering, thereby enhancing thermal radiation exchange at gas–solid interfaces. At the microscale, this structural optimization shortens the radiative transfer path and improves radiative efficiency, resulting in a significant increase in κ_{rad} with increasing *VSSA*. Under the combined influence of conduction and radiation, increasing the VSSA leads to an improvement in κ_{total}, albeit only a slight one, which is likely due to the limited range of surface area values examined in this study.

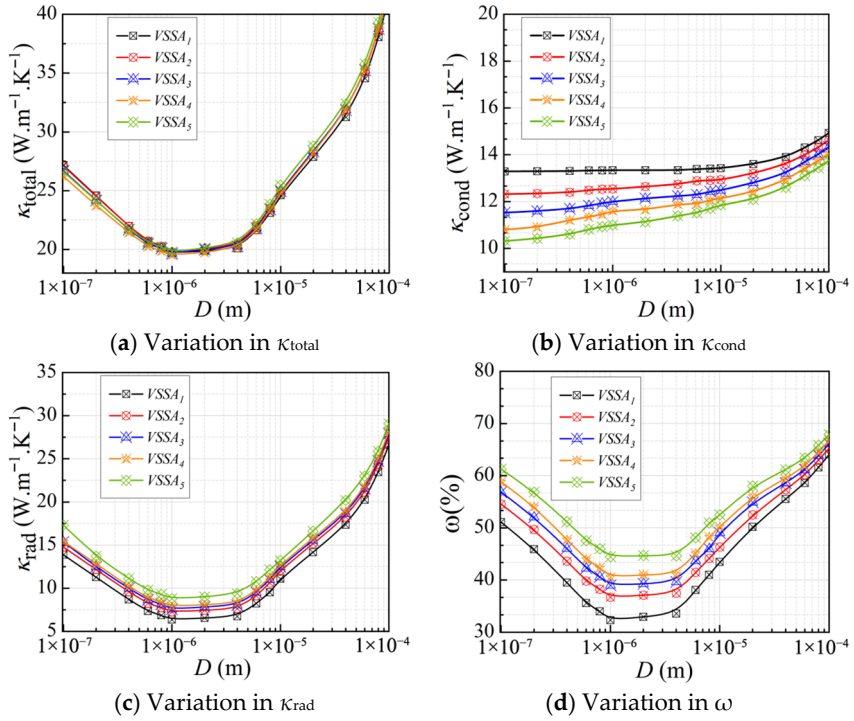

(**a**) Variation in κ_{total} (**b**) Variation in κ_{cond}

(**c**) Variation in κ_{rad} (**d**) Variation in ω

Figure 7. The equivalent thermal conductivity of CMM-gels versus cell size at different volume-to-surface area ratios.

3.2.4. Effect of Material Properties

For mesoporous materials, the radiative thermal conductivity κ_{rad} depends on the relative permittivity ε given by $\varepsilon = (n + ik)^2$, where n is the refractive index and k is the extinction coefficient [16]. In this study, n and k are varied independently to assess their separate effects on the κ_{rad}, with one parameter held constant while the other changes with wavelength. In the following calculations, five models with different n and k were selected to examine the impact on the κ_{total} of CMM-gels at T = 300 K and φ = 90%. Here, n_1 refers to the wavelength-dependent refractive index data from Rakić's experimental data [52]. Similarly, n_2, n_3, n_4, and n_5 are defined as two, three, four, and five times the value of n_1 at each wavelength, respectively, and the corresponding variation trends are shown in Figure 8.

Since changes in refractive index, as a component of relative permittivity, mainly influence electromagnetic wave propagation, their effect on conductive heat transfer is negligible. As shown in Figure 8, a higher n leads to greater internal refraction and reflection, making radiative transfer more sensitive to optical property variations. Thus, materials with higher n reflect more radiative energy, reducing transmission and the effective radiative path within the structure. This diminishes the efficiency of radiative heat transport and results in lower κ_{rad}. When n is increased up to five times its baseline as n_5, κ_{total} consistently reaches a pronounced minimum within the D_h range of approximately 0.6 μm to 2 μm, forming a stable conductivity valley, remaining large changes in n.

Likewise, five model groups with extinction coefficients are set separately; k_1 denotes the extinction coefficient data from Rakić's experimental data [52] as a function of wavelength, while k_2, k_3, k_4, and k_5 represent two, three, four, and five times k_1 at each wavelength, and the corresponding variation trends are shown in Figure 9.

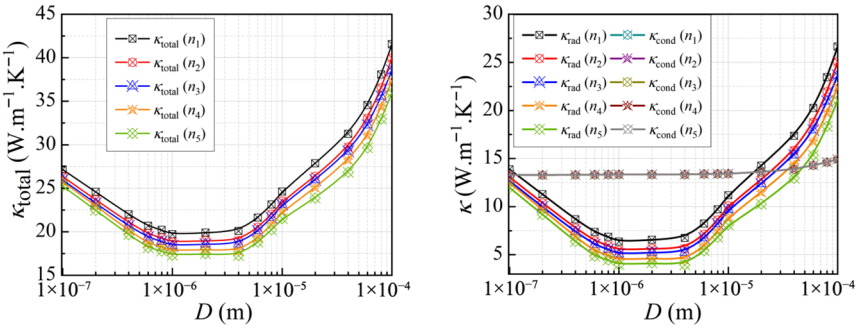

(**a**) Variation of κ_{total} (**b**) Variation of κ_{cond} and κ_{rad}

Figure 8. The equivalent thermal conductivity of CMM-gels versus the cell size at different refractive indexes.

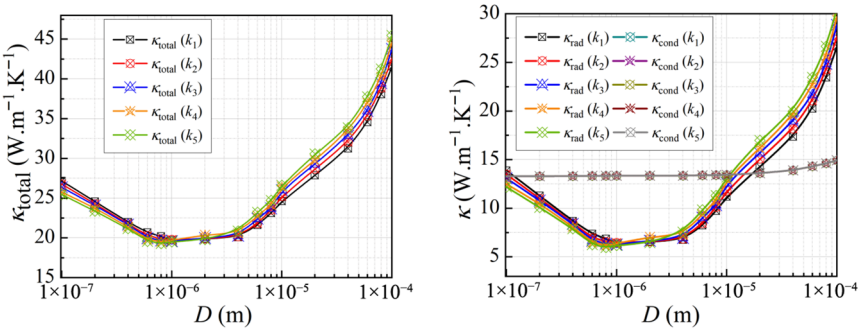

(**a**) Variation in κ_{total} (**b**) Variation in κ_{cond} and κ_{rad}

Figure 9. The equivalent thermal conductivity of CMM-gels versus the cell size at different extinction coefficients.

At the microscale, the effect of the k on the κ_{rad} shows a distinct dependence on the D_h. When the D_h > 10 μm, increasing the k leads to higher κ_{rad}. Conversely, as the D_h decreases, a higher k results in a reduction of κ_{rad}. This phenomenon is attributed to the fact that larger D_h values provide longer radiative transfer paths, allowing radiation to propagate more efficiently and thereby enhancing κ_{rad}. In contrast, when D_h is small, the shortened path increases the frequency of internal reflection and scattering, which confines thermal energy within the reduced κ_{rad}.

3.3. Spectral Radiative Properties

To investigate the thermal radiative properties of the CMM-gels, a series of regular models were constructed based on the occurrence of minimum κ_{total} at D_h = 10 μm and D_h = 1 μm, under porosities of φ = 90%, φ = 80%, and φ = 70%, respectively. The spectral radiative properties, including absorptivity A and reflectivity R, were calculated over the visible and infrared wavelength ranges, with the results as shown in Figure 10.

As shown in Figure 10, the CMM-gel structures exhibit consistent spectral trends across all wavelengths. For example, at porosities of 90% and 80% with D_h = 1 μm, both R and A display pronounced oscillations below 2.5 μm. In the CMM-gels, A is high in the short-wavelength region and then decreases with fluctuations as the wavelength increases, while R transitions from an initial minimum to near-total reflection at longer wavelengths. For D_h = 10 μm, similar behavior is observed, with A rising sharply before 2.5 μm and then

dropping, and R showing a corresponding increase. At longer wavelengths, both A and T are negligible compared to R. These results demonstrate the strong spectral tunability of CMM-gel structures.

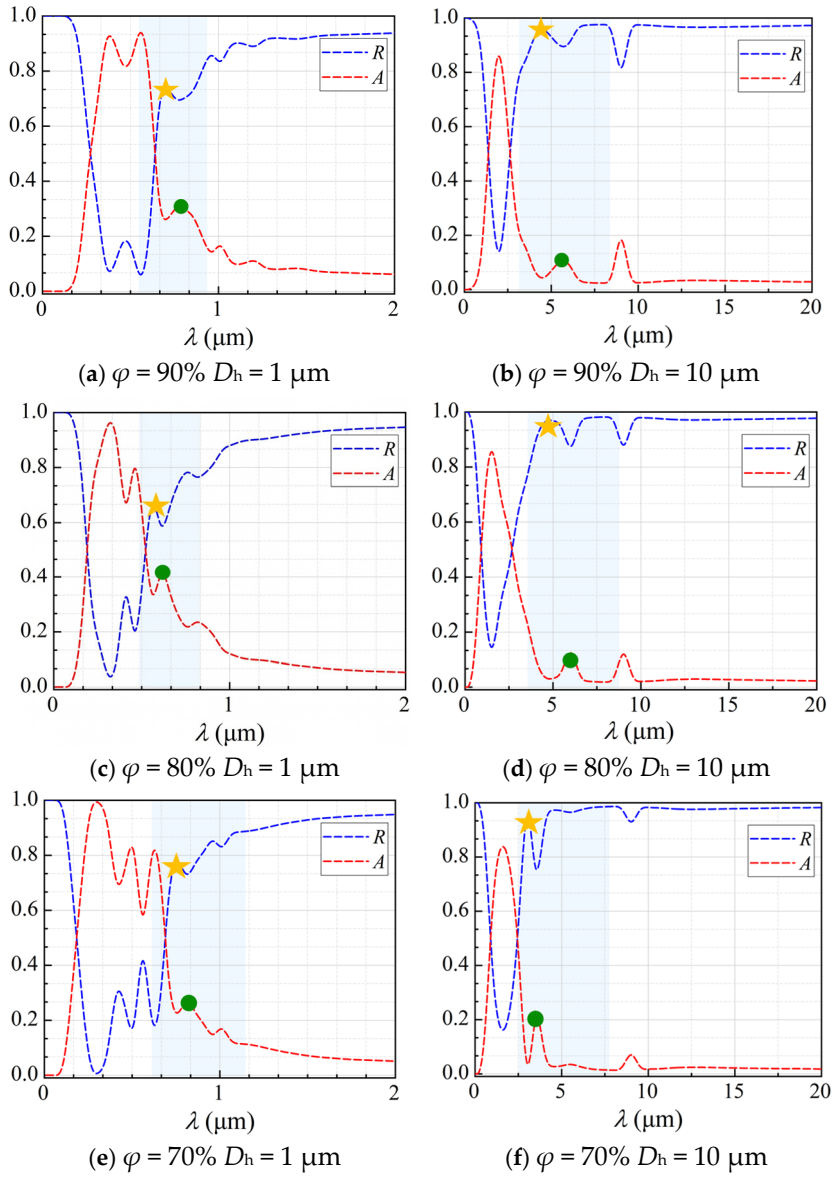

Figure 10. The spectral radiative properties of CMM-gels at minimum κ_{total}.

To further clarify the mechanisms underlying the observed spectral peaks, models with D_h values of 10 μm and 1 μm and porosities of 90%, 80%, and 70% were analyzed, as shown in Figure 11. For D_h = 1 μm, electric and magnetic field distributions were extracted at Z = 0 μm, 0.5 μm, and 1 μm; for D_h = 10 μm, field distributions were obtained at Z = 0 μm, 5 μm, and 10 μm.

The positions of the R and A peaks within the computational domain were determined by tracking the wavelengths at which these maxima occur. Changes in magnetic field intensity and electric field orientation were recorded from the pore edge to the center. Furthermore, analysis of the energy flux at the gas–solid interface enabled the calculation of radiative dissipation efficiency, as illustrated in Figures 12–16.

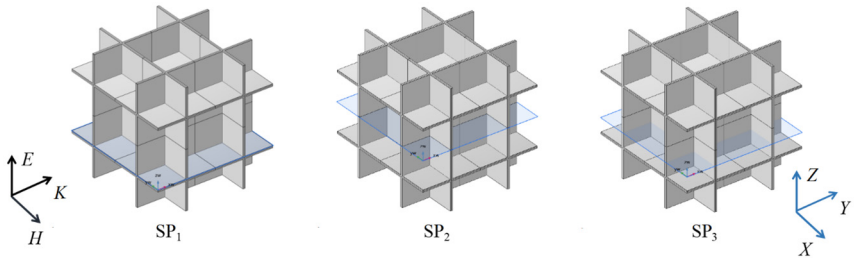

Figure 11. Cross-section schematic.

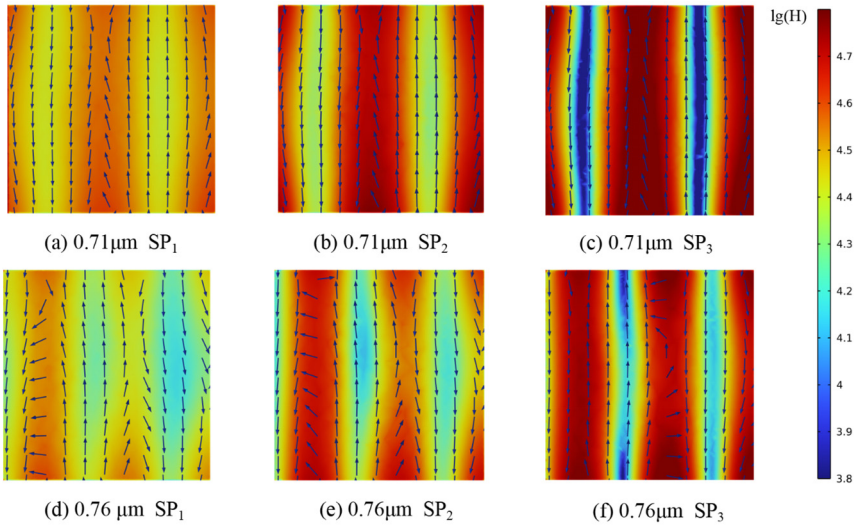

Figure 12. Magnetic field strength and electric field distribution; φ = 90%, D_h = 1 μm.

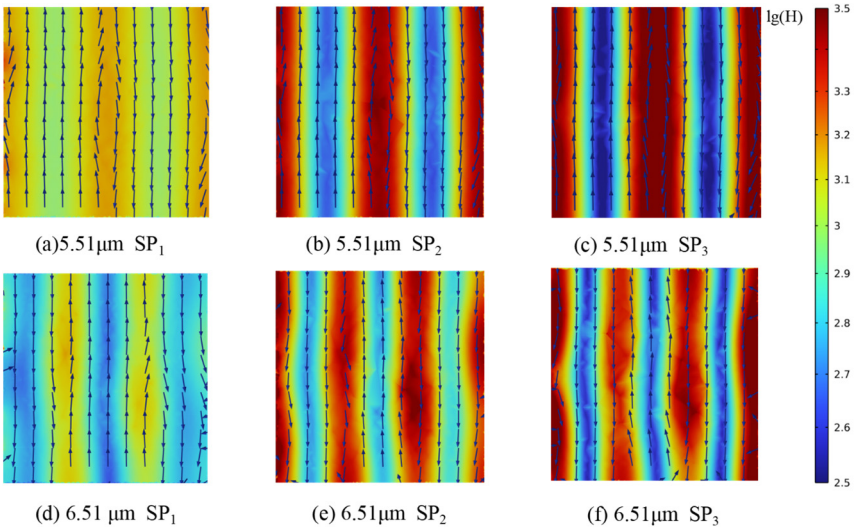

Figure 13. Magnetic field strength and electric field distribution; φ = 90%, D_h = 10 μm.

Magnetic field enhancement regions are always associated with changes in electric field direction, which appear throughout the interior of the closed-cell structure due to the combined effects of surface plasmon resonance and magnetic resonance. Surface plasmon resonance at the gas–solid interface concentrates electromagnetic energy and deflects the electric field, while magnetic resonance causes local suppression of the magnetic field. These phenomena produce characteristic field patterns and magnetic field bands, as illustrated in Figures 12–16. In CMM-gels, most variations in electromagnetic field intensity and direction occur inside the structure. For quantitative comparison, the radiative dissipation efficiency η_{rad} was denoted as $\eta_{\mathrm{rad}} = S_{\mathrm{s}}/S_{\mathrm{m}}$, which is calculated as the ratio of the internal gas-phase energy flux S_{s} to the

total cross-sectional energy flux S_m, enabling direct quantitative comparison across different model configurations. The η_{rad} of each cross-section is shown in Table 1.

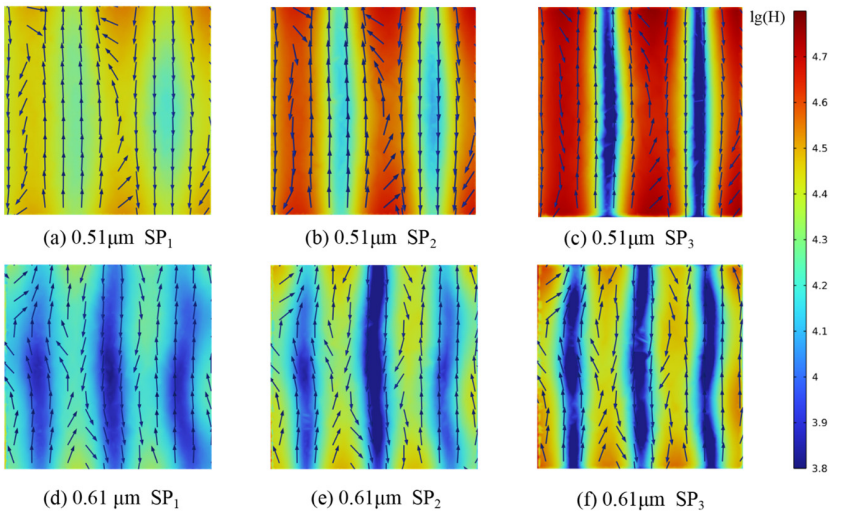

Figure 14. Magnetic field strength and electric field distribution; φ = 80%, D_h = 1 μm.

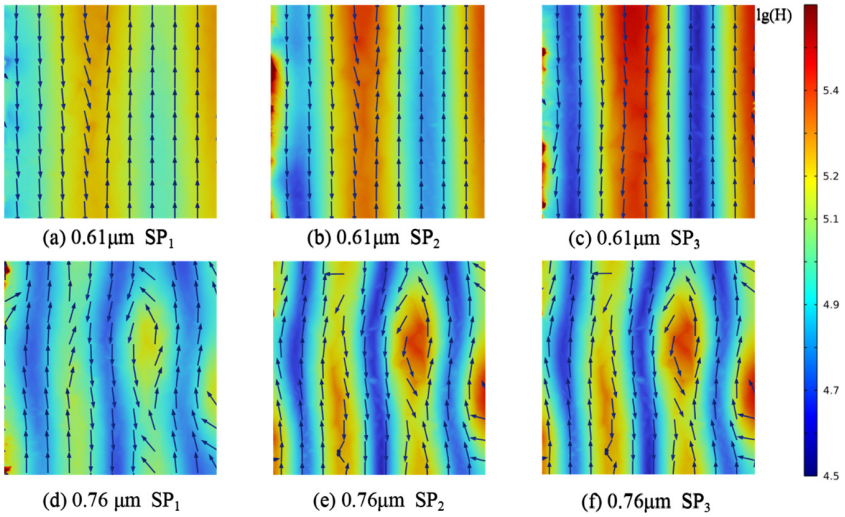

Figure 15. Magnetic field strength and electric field distribution; φ = 70%, D_h = 1 μm.

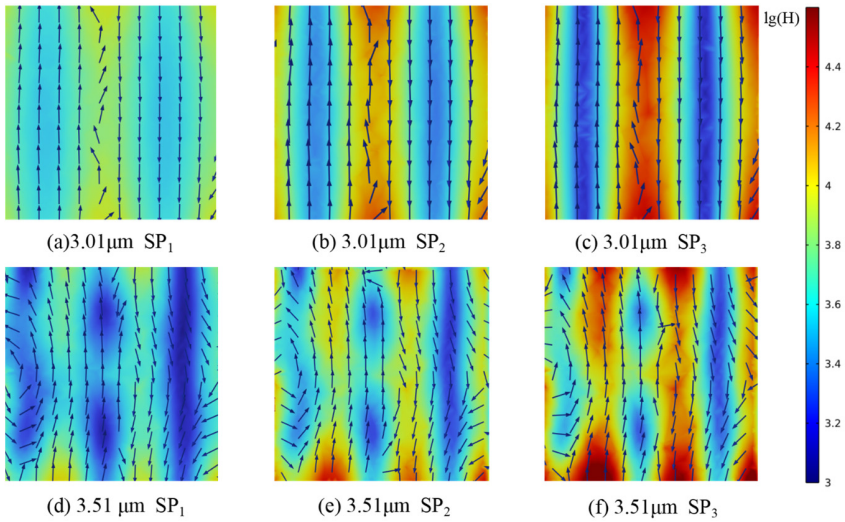

Figure 16. Magnetic field strength and electric field distribution; φ = 70%, D_h = 10 μm.

Table 1. Radiation dissipation efficiency η_{rad} at different cross-sections.

λ	SP_1	SP_2	SP_3	φ	D_h
0.71 μm	24.43	29.13	36.75	90%	1 μm
0.76 μm	30.88	34.43	42.78		
5.51 μm	10.72	12.46	23.28		10 μm
6.51 μm	20.69	22.34	29.90		
0.51 μm	27.24	32.53	42.16	80%	1 μm
0.61 μm	28.87	36.39	49.07		
5.01 μm	18.07	23.3	30.33		10 μm
6.01 μm	22.73	27.84	33.39		
0.61 μm	29.42	34.71	45.66	70%	1 μm
0.76 μm	31.34	36.75	49.43		
3.01 μm	18.27	26.13	38.37		10 μm
3.51 μm	24.87	29.67	45.87		

As shown in Table 1, analysis of structures with varying D_h and φ shows that as D_h decreases, electromagnetic wave propagation paths shorten, leading to more concentrated magnetic field enhancement and more frequent electric field perturbations. The number of pronounced magnetic field bands also increases in smaller D_h. Moving from the edge to the center of the cross-section, the variation in the electromagnetic field becomes more intense, indicating that radiative effects are strongest near the central region of the structure. By comparing the η_{rad} among the models, it is observed that higher φ results in a higher η_{rad}, while at the same φ, larger D_h yields higher η_{rad}. Enhanced internal radiative dissipation reduces κ_{total} by increasing thermal energy loss. These findings confirm that microscale phenomena such as surface plasmon resonance and magnetic resonance are critical for tuning heat transfer properties in CMM-gels and that structural design and material selection enable precise control of both thermal conductivity and electromagnetic response for advanced thermal management applications.

4. Conclusions

In this study, a numerical method combining a Voronoi-based prediction model, the Knudsen effect, and microscale electromagnetic interactions was developed to investigate the effective thermal conductivity and internal heat transfer mechanisms of closed mesoporous metal gels. The model predictions showed close agreement with experimental data, with a maximum deviation of 8.6% and an average error of 5.35%. Systematic parametric analysis revealed clear dependencies of effective thermal conductivity on porosity, pore size, temperature, and optical parameters. Electromagnetic field simulations further identified that surface plasmon resonance and magnetic resonance at the gas–solid interface play a key role in enhancing radiative dissipation. The main findings are as follows:

- The developed numerical model predicts the effective thermal conductivity, within 8.6% error compared with experimental measurements.
- Effective thermal conductivity decreases with increasing porosity, increases with temperature, and reaches a stable minimum at a pore size of about 1 μm. The effects of refractive index, extinction coefficient, and surface area are comparatively minor.
- Electromagnetic resonance phenomena, including surface plasmon and magnetic resonance at the gas–solid interface, significantly enhance internal radiative dissipation and further reduce thermal conductivity.

These effects are amplified in structures with higher porosity and smaller pores, offering clear guidance for the design of next-generation thermal insulation materials.

Author Contributions: Conceptualization, H.Y., M.D. and H.Z.; methodology, M.D.; validation, N.G., A.C. and M.L.; formal analysis, H.Y. and H.Z.; resources, H.Y.; data curation, N.G.; writing—original draft preparation, H.Y.; writing—review and editing, H.Y.; funding acquisition, H.Y. All authors have read and agreed to the published version of the manuscript.

Funding: This research was funded by National Natural Science Foundation of China (No. 52406102) and Shandong Provincial Natural Science Foundation (No. ZR2023QE258).

Institutional Review Board Statement: Not applicable.

Informed Consent Statement: Not applicable.

Data Availability Statement: The original contributions presented in this study are included in the article. Further inquiries can be directed to the corresponding authors.

Acknowledgments: The authors are grateful to the National Natural Science Foundation of China (Grant No. 52406102) and the Shandong Provincial Natural Science Foundation (Grant No. ZR2023QE258). Moreover, the National Natural Science Foundation of China (Grant No. 52406102) sponsored the publication fee of this paper.

Conflicts of Interest: There are no conflicts to declare.

References

1. Lei, S.; Hu, C.; Li, Z.; Tan, S.; Wang, C.; Wu, Y. Boiling heat transfer enhancement on heterogeneous copper foams in the presence of transverse flow. *Appl. Therm. Eng.* **2025**, *260*, 124990.
2. Palombo, M.; Barbetta, A.; Cametti, C.; Favero, G.; Capuani, S. Transient Anomalous Diffusion MRI Measurement Discriminates Porous Polymeric Matrices Characterized by Different Sub-Microstructures and Fractal Dimension. *Gels* **2022**, *8*, 95. [CrossRef]
3. Chai, J.; Wang, G.; Wang, G.; Shao, R.; Zhao, J.; Zhao, G.; Park, C.B. Porous and Conductive Fiber Woven Textile for Multi-Functional Protection, Personal Warmth, and Intelligent Motion/Temperature Perception. *Adv. Funct. Mater.* **2025**, *35*, 2416428.
4. Singh, A.; Rangarajan, S.; Sammakia, B. Utilizing Ragone framework for optimized phase change material-based heat sink design in electronic cooling applications. *Int. J. Heat Mass Transf.* **2024**, *227*, 125518. [CrossRef]
5. Aichmayer, L.; Garrido, J.; Wang, W.; Berg, J.; Vlaskin, A.; Guo, Z.; Tallaire, A.; Stöhr, R.; Rüde, U. Experimental evaluation of a novel solar receiver for a micro gas-turbine based solar dish system in the KTH high-flux solar simulator. *Energy* **2018**, *159*, 184–195.
6. Yu, H.; Zhang, H.; Zhao, J.; Liu, J.; Xia, X.; Wu, X. Thermal conductivity of micro/nano-porous polymers: Prediction models and applications. *Front. Phys.* **2022**, *17*, 1–19. [CrossRef]
7. Yu, H.; Zhang, H.; Buahom, P.; Liu, J.; Xia, X.; Park, C.B. Prediction of thermal conductivity of micro/nano porous dielectric materials: Theoretical model and impact factors. *Energy* **2021**, *233*, 121140. [CrossRef]
8. Gong, P.; Wang, G.; Tran, M.P.; Buahom, P.; Zhai, S.; Li, G.; Park, C.B. Advanced bimodal polystyrene/multi-walled carbon nanotube nanocomposite foams for thermal insulation. *Carbon* **2017**, *120*, 1–10.
9. Wang, G.; Wang, C.; Zhao, J.; Wang, G.; Park, C.B.; Zhao, G.; Janssen, H. Correction: Modelling of thermal transport through a nanocellular polymer foam: Toward the generation of a new superinsulating material. *Nanoscale* **2018**, *10*, 20469–20473. [CrossRef]
10. Buahom, P.; Wang, C.; Alshrah, M.; Wang, G.; Gong, P.; Tran, M.P.; Park, C.B. Wrong expectation of superinsulation behavior from largely-expanded nanocellular foams. *Nanoscale* **2020**, *12*, 13064–13085. [CrossRef]
11. Notario, B.; Pinto, J.; Solorzano, E.; de Saja, J.A.; Dumon, M.; Rodríguez-Pérez, M.A. Experimental validation of the Knudsen effect in nanocellular polymeric foams. *Polymer* **2015**, *56*, 57–67. [CrossRef]
12. Bernardo, V.; Martin-de Leon, J.; Pinto, J.; Verdejo, R.; Rodriguez-Perez, M.A. Modeling the heat transfer by conduction of nanocellular polymers with bimodal cellular structures. *Polymer* **2019**, *160*, 126–137. [CrossRef]
13. Chaichi, M.; Bahramian, A.R. Theoretical relation of the structure and thermal properties of gradient thermal insulator aerogels using fractal geometry. *Microporous Mesoporous Mater.* **2022**, *333*, 111722. [CrossRef]
14. Yu, H.; Li, M.; Guo, N.; Chen, A.; Zhang, H.; Du, M. Fractal-Based Thermal Conductivity Prediction Modeling for Closed Mesoporous Polymer Gels. *Gels* **2025**, *11*, 391. [CrossRef]
15. Yu, H.; Zhang, H.; Xia, X. A fractal-skeleton model of high porosity macroporous aluminum and its heat transfer characterizes. *J. Therm. Anal. Calorim.* **2020**, *141*, 351–360. [CrossRef]
16. Han, Y.F.; Xia, X.L.; Tan, H.P.; Liu, H.D. Modeling of phonon heat transfer in spherical segment of silica aerogel grains. *Phys. B Condens. Matter* **2013**, *420*, 58–63. [CrossRef]
17. Zeng, T.; Liu, W. Phonon heat conduction in micro-and nano-core-shell structures with cylindrical and spherical geometries. *J. Appl. Phys.* **2003**, *93*, 4163–4168. [CrossRef]

18. Xie, T.; He, Y.L. Heat transfer characteristics of silica aerogel composite materials: Structure reconstruction and numerical modeling. *Int. J. Heat Mass Transf.* **2016**, *95*, 621–635. [CrossRef]
19. Sean, D.; Landsgesell, J.; Holm, C. Computer simulations of static and dynamical properties of weak polyelectrolyte nanogels in salty solutions. *Gels* **2017**, *4*, 2. [CrossRef]
20. El Hajj, S.; Ntaté, M.B.; Breton, C.; Siadous, R.; Aid, R.; Dupuy, M.; David, B. Bone Spheroid Development Under Flow Conditions with Mesenchymal Stem Cells and Human Umbilical Vein Endothelial Cells in a 3D Porous Hydrogel Supplemented with Hydroxyapatite. *Gels* **2024**, *10*, 666. [CrossRef]
21. Zhang, Z.M. *Nano/Microscale Heat Transfer*; Springer International Publishing: Berlin/Heidelberg, Germany, 2024.
22. Shen, S.; Narayanaswamy, A.; Chen, G. Surface phonon polaritons mediated energy transfer between nanoscale gaps. *Nano Lett.* **2009**, *9*, 2909–2915. [CrossRef]
23. Howell, J.R.; Siegel, R.; Mengüç, M.P. *Thermal Radiation Heat Transfer*, 5th ed.; CRC Press, Taylor & Francis Group: Boca Raton, FL, USA, 2010.
24. Pozar, D.M. *Microwave Engineering*; Wiley: Hoboken, NJ, USA, 2001.
25. Tan, H.; Liu, L.; Yi, H.; Zhao, J.; Qi, H.; Tan, J. Recent progress in computational thermal radiative transfer. *Chin. Sci. Bull.* **2009**, *54*, 4135–4147. [CrossRef]
26. Jin, Y.; Wu, Y.; Li, H.; Zhao, M.; Pan, J. Definition of fractal topography to essential understanding of scale-invariance. *Sci. Rep.* **2017**, *7*, 46672. [CrossRef] [PubMed]
27. Vacher, R.; Woignier, T.; Pelous, J.; Courtens, E. Structure and self-similarity of silica aerogels. *Phys. Rev. B* **1988**, *37*, 6500. [CrossRef] [PubMed]
28. Paun, M.A.; Paun, V.A.; Paun, V.P. Acoustic fractional propagation in terms of porous xerogel and fractal parameters. *Gels* **2024**, *10*, 83. [CrossRef] [PubMed]
29. Hayase, Y.; Ohta, T. Sierpinski gasket in a reaction-diffusion system. *Phys. Rev. Lett.* **1998**, *81*, 1726. [CrossRef]
30. Ma, Y.; Yu, B.; Zhang, D.; Zou, M. A self-similarity model for effective thermal conductivity of porous media. *J. Phys. D Appl. Phys.* **2003**, *36*, 2157. [CrossRef]
31. Liu, H.; Liu, J.A.; Tian, Y.; Jiao, J.; Wu, X. Thermal insulation performance of silica aerogel composites doped with hollow opacifiers: Theoretical approach. *Gels* **2022**, *8*, 295. [CrossRef]
32. Okabe, A.; Boots, B.; Sugihara, K.; Chiu, S.N. *Spatial Tessellations: Concepts and Applications of Voronoi Diagrams*; Wiley: Hoboken, NJ, USA, 2009.
33. Notario, B.; Pinto, J.; Rodriguez-Perez, M.A. Nanoporous polymeric materials: A new class of materials with enhanced properties. *Prog. Mater. Sci.* **2016**, *78*, 93–139. [CrossRef]
34. Chen, A.; Chai, J.; Ren, X.; Li, M.; Yu, H.; Wang, G. A Novel Prediction Model for Thermal Conductivity of Open Microporous Metal Foam Based on Resonance Enhancement Mechanisms. *Energies* **2025**, *18*, 1529. [CrossRef]
35. Lin, Z.; Lan, Y.; Huang, C. Reduced thermal conductivity of nanoparticle packed bed by hybrid design. *Int. J. Heat Mass Transf.* **2020**, *162*, 120340. [CrossRef]
36. Lin, Z.Z.; Huang, C.L.; Luo, D.C.; Feng, Y.H.; Zhang, X.X.; Wang, G. Thermal performance of metallic nanoparticles in air. *Appl. Therm. Eng.* **2016**, *105*, 686–690. [CrossRef]
37. Singh, R.; Kasana, H.S. Computational aspects of effective thermal conductivity of highly porous metal foams. *Appl. Therm. Eng.* **2004**, *24*, 1841–1849. [CrossRef]
38. Shen, S.; Henry, A.; Tong, J.; Zheng, R.; Chen, G. Polyethylene nanofibres with very high thermal conductivities. *Nat. Nanotechnol.* **2010**, *5*, 251–255. [CrossRef] [PubMed]
39. Liu, X.; Wang, L.; Zhang, Z.M. Near-field thermal radiation: Recent progress and outlook. *Nanoscale Microscale Thermophys. Eng.* **2015**, *19*, 98–126. [CrossRef]
40. Rytov, S.M.; Kravtsov, Y.A.; Tatarskii, V.I. *Principles of Statistical Radiophysics*; Springer: Berlin/Heidelberg, Germany, 1987.
41. Basu, S.; Zhang, Z.M.; Fu, C.J. Review of near-field thermal radiation and its application to energy conversion. *Int. J. Energy Res.* **2009**, *33*, 1203–1232. [CrossRef]
42. Wu, X.; Fu, C.; Zhang, Z.M. Effect of orientation on the directional and hemispherical emissivity of hyperbolic metamaterials. *Int. J. Heat Mass Transf.* **2019**, *135*, 1207–1217. [CrossRef]
43. Bernardo, V.; Martin-de Leon, J.; Pinto, J.; Schade, U.; Rodriguez-Perez, M.A. On the interaction of infrared radiation and nanocellular polymers: First experimental determination of the extinction coefficient. *Colloids Surf. A Physicochem. Eng. Asp.* **2020**, *600*, 124937. [CrossRef]
44. Martín-de León, J.; Pura, J.L.; Bernardo, V.; Rodríguez-Pérez, M.Á. Transparent nanocellular PMMA: Characterization and modeling of the optical properties. *Polymer* **2019**, *170*, 16–23. [CrossRef]
45. Mayerhöfer, T.G.; Pahlow, S.; Popp, J. The Bouguer-Beer-Lambert law: Shining light on the obscure. *ChemPhysChem* **2020**, *21*, 2029–2046. [CrossRef]

46. Pelissari, P.I.; Angélico, R.A.; Salvini, V.R.; Vivaldini, D.O.; Pandolfelli, V.C. Analysis and modeling of the pore size effect on the thermal conductivity of alumina foams for high temperature applications. *Ceram. Int.* **2017**, *43*, 13356–13363. [CrossRef]
47. Zhao, L. Radiative Transport in Transparent Aerogels for Solar Thermal Energy Applications. Doctoral Dissertation, Massachusetts Institute of Technology, Cambridge, MA, USA, 2019.
48. Solórzano, E.; Reglero, J.A.; Rodríguez-Pérez, M.A.; Lehmhus, D.; Wichmann, M.; De Saja, J.A. An experimental study on the thermal conductivity of aluminium foams by using the transient plane source method. *Int. J. Heat Mass Transf.* **2008**, *51*, 6259–6267. [CrossRef]
49. Calmidi, V.V.; Mahajan, R.L. The effective thermal conductivity of high porosity fibrous metal foams. *J. Heat Transf.* **1999**, *121*, 466–471. [CrossRef]
50. Paek, J.W.; Kang, B.H.; Kim, S.Y.; Hyun, J.M. Effective thermal conductivity and permeability of aluminum foam materials. *Int. J. Thermophys.* **2000**, *21*, 453–464. [CrossRef]
51. Takegoshi, E.; Hirasawa, Y.; Matsuo, J.; Okui, K. A study on effective thermal conductivity of porous metals. *Trans. Jpn. Soc. Mech. Eng. Ser. B* **1992**, *58*, 879–884. [CrossRef]
52. Rakić, A.D. Algorithm for the determination of intrinsic optical constants of metal films: Application to aluminum. *Appl. Opt.* **1995**, *34*, 4755–4767. [CrossRef]